

Deformable Endoscopic Tissues Reconstruction with Gaussian Splatting

Lingting Zhu¹, Zhao Wang², Zhenchao Jin¹, Guying Lin¹, and Lequan Yu¹ (✉)

¹ The University of Hong Kong, Hong Kong SAR, China
ltzhu99@connect.hku.hk lqyu@hku.hk

² The Chinese University of Hong Kong, Hong Kong SAR, China

Abstract. Surgical 3D reconstruction is a critical area of research in robotic surgery, with recent works adopting variants of dynamic radiance fields to achieve success in 3D reconstruction of deformable tissues from single-viewpoint videos. However, these methods often suffer from time-consuming optimization or inferior quality, limiting their adoption in downstream tasks. Inspired by 3D Gaussian Splatting, a recent trending 3D representation, we present EndoGS, applying Gaussian Splatting for deformable endoscopic tissue reconstruction. Specifically, our approach incorporates deformation fields to handle dynamic scenes, depth-guided supervision to optimize 3D targets with a single viewpoint, and a spatial-temporal weight mask to mitigate tool occlusion. As a result, EndoGS reconstructs and renders high-quality deformable endoscopic tissues from a single-viewpoint video, estimated depth maps, and labeled tool masks. Experiments on DaVinci robotic surgery videos demonstrate that EndoGS achieves superior rendering quality. Code is available at <https://github.com/HKU-MedAI/EndoGS>.

Keywords: Gaussian Splatting · Robotic Surgery · 3D Reconstruction

1 Introduction

Reconstruction high-quality deformable tissues from endoscopic videos is a significant but challenging task, facilitating downstream tasks like surgical AR, education, and robot learning [3, 22, 23]. Earlier attempts [13, 20, 24, 32, 33] adopt depth estimation to achieve great success in endoscopic reconstruction, but these methods still struggle to produce realistic 3D reconstruction due to two key issues. First, non-rigid deformations with sometimes large movements, which require practical dynamic scene reconstruction, hinders the adaptation of those techniques. Second, tool occlusion happens in single-viewpoint videos, producing difficulties in learning affected parts with limited information.

While [9, 12] have proposed frameworks combining tool masking, stereo depth estimation, and sparse warp field [6, 16] for single-viewpoint 3D reconstruction, they are still prone to failure in the presence of dramatic non-topological deformable tissues changes. Neural Radiance Fields (NeRFs) [15] have shown great

potentials in 3D representations, and methods based on variants of dynamic radiance field [5, 18] have become representative works in deformable tissues reconstruction from videos. For example, EndoNeRF [25] follows the modeling of D-NeRF [18] to represent deformable surgical scenes as the combination of a canonical neural radiance field and a time-dependent neural displacement field, and LerPlane [28] factorizes six 2D planes for static field and dynamic field to accelerate optimization similar to [2, 5]. There is also a growing interest to reconstruct surfaces from endoscopic videos via neural implicit fields [1, 31].

Recently 3D Gaussian Splatting (3D-GS) [8] has been witnessed as a powerful representation that renders higher-quality results at a real-time level. Follow-up works [14, 26, 29, 30] extend 3D-GS to represent dynamic scenes and achieve state-of-the-art performances on rendering fidelity and speed. To model dynamic representation of dynamic scenes, [14, 29] formulate 4D Gaussians and assign extra parameters as attributes in the time dimension, and [26, 30] apply MLPs to predict the deformation of the Gaussians, sharing the same rationale with dynamic NeRFs [17, 18]. In this paper, we present EndoGS, a method based on Gaussian Splatting for high-fidelity rendering of deformable endoscopic tissues reconstruction with better rendering quality and better rendering speed.

To summarize, our main contributions are three-fold: **1)** We present a novel Gaussian Splatting based method for deformable endoscopic tissues reconstruction. This is one of the first attempts [10] introducing Gaussian Splatting in the medical domain. **2)** We represent dynamic surgical scenes with the combination of static Gaussians and the deformable parameters in the time dimension, adopt depth-guided supervision for monocular optimization, and apply a spatial-temporal weight mask to mitigate tool occlusion. Besides, we also introduce total variation items to mitigate quality degradation in the spatial domain as well as in the temporal domain. **3)** While former works [25, 27, 28] apply tool masks to filter out un-desired parts and evaluate the rendered visible pixels with the ground-truth, different training masks are adopted for metrics evaluation. To this end, we use the same input masks involved in the training and inference for comparison methods and make a clear and fair comparison on rendered video quality.

2 Method

2.1 Overview

In this paper, we introduce our method, referred to as EndoGS, which utilizes a deformable variant of 3D-GS to reconstruct 3D surgical scenes from a single-viewpoint video, estimated depth maps, and labeled tool masks. Specifically, given a stereo video with left and right frames $\{(\mathbf{I}_i^l, \mathbf{I}_i^r)\}_{i=1}^T$, where T is the total number of frames, our goal is to reconstruct 3D representations of the deformable tissues that render in high quality. We follow the approach of [25, 27, 28] by combining the extracted binary tool masks $\{\mathbf{M}_i\}_{i=1}^T$ and the depth maps $\{\mathbf{D}_i\}_{i=1}^T$ estimated from binocular captures for the left views. The pipeline of EndoGS is illustrated in Fig. 1. In this section, we first introduce the preliminary of 3D

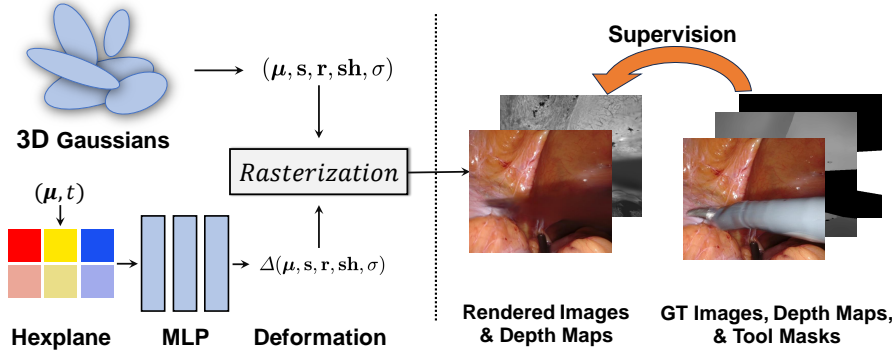


Fig. 1. The overview of our EndoGS pipeline. Given 3D Gaussians, we use the mean and the time as input to compute features by querying multi-resolution voxel planes. A single MLP is used to obtain the deformation of the Gaussians. With differentiable rasterization, the rendered images and depth maps are obtained and we use ground truth images, depth maps and the tool masks to provide the supervision.

Gaussian Splatting (Section 2.2). We then present the modeling of deformable tissues with a dynamic version of 3D-GS, which adopts a lightweight MLP to represent the dynamic field (Section 2.3). Finally, the training optimization of the Gaussian Splatting with the tool masks and the depth maps is introduced (Section 2.4).

2.2 Preliminaries of 3D Gaussian Splatting

3D Gaussian Splatting (3D-GS) [8] offers the state-of-the-art solution for real-time novel view synthesis in multi-view static scenes. The 3D Gaussians with a 3D covariance matrix Σ and mean μ served as the rendering primitives in the form of point clouds:

$$G(\mathbf{x}) = e^{-\frac{1}{2}(\mathbf{x}-\mu)^T \Sigma^{-1}(\mathbf{x}-\mu)}. \quad (1)$$

The 3D Gaussians can be projected onto 2D space and rendered for pixels [34]:

$$\Sigma' = \mathbf{J} \mathbf{W} \Sigma \mathbf{W}^T \mathbf{J}^T, \quad (2)$$

where Σ' is the covariance matrix in the 2D plane, \mathbf{W} denotes view transformation, and the Jacobian \mathbf{J} is the affine approximation of the projective transformation. To enforce the positive semi-definiteness, Σ is parameterized with a scale \mathbf{S} and rotation \mathbf{R} :

$$\Sigma = \mathbf{R} \mathbf{S} \mathbf{S}^T \mathbf{R}^T. \quad (3)$$

To render the color of the pixels \mathbf{p} , point-based volume rendering is adopted:

$$C(\mathbf{p}) = \sum_{i \in N} c_i \alpha_i \prod_{j=1}^{i-1} (1 - \alpha_j), \quad (4)$$

$$\text{where } \alpha_i = \sigma_i e^{-\frac{1}{2}(\mathbf{p} - \boldsymbol{\mu}_i)^T \boldsymbol{\Sigma}'^{-1}(\mathbf{p} - \boldsymbol{\mu}_i)}. \quad (5)$$

The c_i means the color of the Gaussians along the ray, $\boldsymbol{\mu}_i$ denotes the coordinates, and σ_i denotes the opacity. And 3D-GS applies spherical harmonics [19] to model the view-dependent color. In total, the explicit 3D Gaussians are characterized by: position $\boldsymbol{\mu} \in \mathbb{R}^3$, scaling factor $\mathbf{s} \in \mathbb{R}^3$, rotation factor $\mathbf{r} \in \mathbb{R}^4$, spherical harmonic (SH) coefficients $\mathbf{sh} \in \mathbb{R}^k$ (k means number of SH functions), and opacity $\sigma \in \mathbb{R}$. Finally each Gaussian can be represented as $(\boldsymbol{\mu}, \mathbf{s}, \mathbf{r}, \mathbf{sh}, \sigma)$.

2.3 Gaussian Splatting Representations for Deformable Tissues

We represent a surgical scene as a 4D volume, where the deformation of the tissues involves time dimension. To this end, we use introduce the Gaussian deformation to represent the time-varying motions and shapes, following the basic designs of [26]. The final goal is to learn the original representation of the 3D Gaussians $\{(\boldsymbol{\mu}, \mathbf{s}, \mathbf{r}, \mathbf{sh}, \sigma)\}$ as well as the Gaussian deformations $\{\Delta(\boldsymbol{\mu}, \mathbf{s}, \mathbf{r}, \mathbf{sh}, \sigma)\} = \{(\Delta\boldsymbol{\mu}, \Delta\mathbf{s}, \Delta\mathbf{r}, \Delta\mathbf{sh}, \Delta\sigma)\}$.

In Fig. 1, for each 3D Gaussian, we use the mean $\boldsymbol{\mu} = (x, y, z)$ and the time t to compute the deformation. We use six orthogonal feature planes to encode the spatial and temporal information [2, 5, 26–28]. To be specific, the multi-resolution HexPlane [2, 5] consists of three space planes XY, XZ, YZ and three space-time planes XT, YT, ZT . The planes encode features $F \in \mathbb{R}^{h \times N_1 \times N_2}$, where h denotes the hidden dimension and N_1, N_2 stand for the plane resolution, and we utilize bilinear interpolation \mathcal{B} to interpolate the four nearby queried voxel features. As a result, the voxel feature can be represented in the format of matrix element-wise multiplication with operation \odot :

$$f_{voxel}(\boldsymbol{\mu}, t) = \mathcal{B}(F_{XY}, x, y) \odot \mathcal{B}(F_{YZ}, y, z) \dots \mathcal{B}(F_{YT}, y, \tau) \odot \mathcal{B}(F_{ZT}, z, \tau),$$

Then we employ a single MLP to update the Gaussian attributes and it merges all the information and decodes the deformation of the position, scaling factor, rotation factor, spherical harmonic coefficients, and opacity:

$$\Delta(\boldsymbol{\mu}, \mathbf{s}, \mathbf{r}, \mathbf{sh}, \sigma) = \text{MLP}(f_{voxel}(\boldsymbol{\mu}, t)).$$

2.4 Training Combined with Tool Masks and Depth Maps

Reconstructing from videos with tool occlusion poses a challenge and we follow former works [25, 27, 28] to use labeled tool occlusion masks to indicates the unseen pixels. Furthermore, we leverage spatiotemporal importance sampling strategy to indicate the crucial areas related to the occlusion issue. Since we

optimize the Gaussians with spatial targets, we can simply devise weight masks in the spatial domain to serve the optimization losses. To be specific, the binary masks are denoted as $\{\mathbf{M}_i\}_{i=1}^T$, where 0 stands for tissue pixels and 1 stands for tool pixels, and the importance maps $\{\mathbf{V}_i\}_{i=1}^T$ involve temporal statistics and are denoted as

$$\mathbf{V}_i = (\mathbf{1} - \mathbf{M}_i) \odot \left(\mathbf{1} + \alpha \sum_{j=1}^T \mathbf{M}_j / \left\| \sum_{j=1}^T \mathbf{M}_j \right\|_F \right).$$

We only optimize in the seen part by introducing the item $\mathbf{1} - \mathbf{M}_i$. Meanwhile, the statistics of the mask frequencies normalized by the Frobenius norm along the temporal dimension provide the information of the uncertainty and allocate higher importance for tissue areas with higher occlusion frequencies. The parameter α is used to control the scaling strength. We use the L_1 reconstruction loss with spatial masks, and thus the spatial supervision on i -th is:

$$\mathcal{L}_{L1}(i) = |\mathbf{I}_i \odot \mathbf{V}_i - \hat{\mathbf{I}}_i \odot \mathbf{V}_i|,$$

where $\hat{\mathbf{I}}_i$ is the rendering image on i -th frame.

Monocular reconstruction provides limited information for 3D reconstruction and makes overfitting happen with single-viewpoint images [4]. To mitigate illness from single-viewpoint inputs, we introduce depth-guided loss with the estimated depth maps. The coarse stereo depth maps $\{\mathbf{D}_i\}_{i=1}^T$ are obtained via STTR-light [11]. We adopt Huber loss for depth regularization following [28]:

$$\mathcal{L}_D(i) = \begin{cases} 0.5\Delta\mathbf{D}_i^2, & \text{if } |\Delta\mathbf{D}_i| < \delta \\ \delta(\Delta\mathbf{D}_i - 0.5\delta), & \text{otherwise} \end{cases}$$

where $\Delta\mathbf{D}_i = |\mathbf{D}_i - \hat{\mathbf{D}}_i|$ denotes the depth loss at i -th frame, and $\hat{\mathbf{D}}_i$ is the rendering depth.

We adopt total variation (TV) losses in the spatial dimension and the temporal dimension to serve as the additional regularization. To prevent color drifts in unseen area during Gaussians optimization, we use a spatial total variation item for areas with tool masks and it is denoted as $\mathcal{L}_{tv-spatial}(i) = \text{TV}(\hat{\mathbf{I}}_i \odot \mathbf{M}_i)$. And we use the temporal total variation item $\mathcal{L}_{tv-temporal}$ in [26] to regularize the Hexplane optimization. Our final optimization target at i -th frame is:

$$\mathcal{L}(i) = \mathcal{L}_{L1}(i) + \lambda_D \mathcal{L}_D(i) + \lambda_{TV1} \mathcal{L}_{tv-spatial}(i) + \lambda_{TV2} \mathcal{L}_{tv-temporal},$$

where hyperparameters λ_D , λ_{TV1} , and λ_{TV2} control the regularization strength.

3 Experiments

3.1 Datasets and Evaluation Metrics

We evaluate our proposed method on the dataset from [25]: typical robotic surgery videos from 6 cases of DaVinci robotic data. The datasets are designed

Table 1. Quantitative comparison on rendering quality and speed.

Methods	PSNR \uparrow	SSIM \uparrow	LPIPS \downarrow	FPS \uparrow
EndoNeRF [25]	35.624	0.942	0.064	< 0.2
ForPlane [27]	36.457	0.946	0.058	\sim 1.7
EndoGS (Ours)	37.654	0.965	0.036	\sim 40

to capture challenging surgical scenes with non-rigid deformation and tool occlusion. We use standard image quality metrics, including PSNR, SSIM, and LPIPS. Since in evaluation the groundtruth pixels for unseen areas are missing, the tool masks are used to exclude unseen parts for computation and unlike [25, 27, 28], we do not count those pixels in PSNR. We also report the frame per second (FPS) to compare the rendering speed of the methods. Besides, while former works [25, 27, 28] adopt the different tool mask configurations in training and evaluation or compare methods under different configurations, we argue to train and evaluate in the same tool mask configurations to prevent meaningless pixels comparison, and compare methods the same tool occlusion masks.

3.2 Implementation Details

In our approach, we adopt the two-stage training methodology in [26] to model the static and deformation fields. In the first stage, we train 3D Gaussian models for the static field, while in the second stage, we focus on training the deformation field. We conduct 3,000 and 60,000 iterations for the first and second stages, respectively. The initial point clouds are estimated using COLMAP [21]. The importance maps scaling strength α is set to 30 and $\delta = 0.2$ for depth loss. Hyperparameters λ_D , λ_{TV1} , and λ_{TV2} are set to 0.03, 0.01, and 1.0.

3.3 Results

We compare EndoGS against two methods, *i.e.*, EndoNerf [25] and ForPlane [27] (an updated version of LerPlane [28]), due to their competitive rendering quality. ForPlane is trained for 32k iterations. We use the same masks in training and evaluation for three methods and evaluate the rendering results on the same cropped zone where the lowest part of the videos that contain display patterns are removed.

Fig. 2 presents a qualitative comparison on scene "traction" between EndoGS and competitive baselines. On the rendering quality, EndoGS clearly outperforms other methods. Tissues deformation occurs at different timesteps, and our method better reconstructs the deformation along the time. Table 1 presents a quantitative comparison on the 6 videos, showcasing the superior performances of our method over the baseline methods in terms of various evaluation metrics related to rendering quality and speed. Considering that EndoNeRF exhibits poor performance on the first rendering frame, we exclude the first frames from

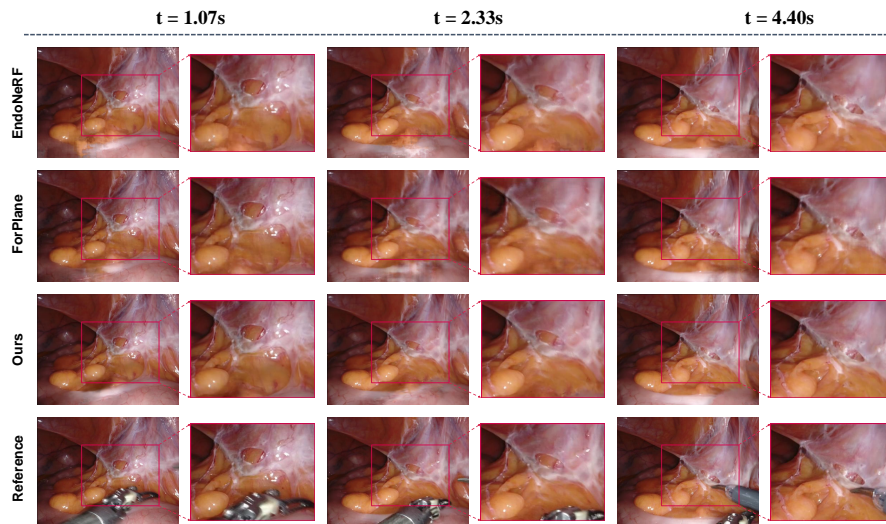


Fig. 2. Qualitative results on scene “traction” at different timesteps.

the evaluation process for all three methods. In terms of rendering quality, EndoGS demonstrates a significant advantage, outperforming the other methods by a considerable margin. Furthermore, EndoGS benefits from the rendering efficiency of Gaussian Splatting, enabling it to achieve real-time rendering speeds. In contrast, the baseline methods struggle to maintain a high FPS rate, highlighting the superiority of EndoGS in this regard.

Ablation Analysis. Fig. 3 presents the ablation study on depth regularization. While we optimize the Gaussians from a single-viewpoint video, 3D information is missing and it is likely the representations are overfitted. We leverage estimated depth maps to help mitigate the illness. It is shown that without depth regularization or with a smaller weight of the regularization, the rendered depth maps are strayed away from the depth guidance. In Fig. 4, we show the effectiveness of spatial Total Variation loss. While we optimize the Gaussians on seen pixels in frames with the tool masks, the lack of continuity leads to color drift in rendering results (frame w/o spatial TV). This phenomenon can be mitigated during the optimization with spatial TV loss.

4 Conclusion

We present a method based on Gaussian Splatting for deformable endoscopic tissues reconstruction, rendering high-quality deformable tissues in real-time from a single-viewpoint video, estimated depth maps, and labeled tool masks. Experiments on DaVinci robotic surgery videos show higher rendering quality.

Limitations and Future Works. Our work has limitations in two folds. First, 3D reconstruction from single-viewpoints videos is an ill-posed problem, making

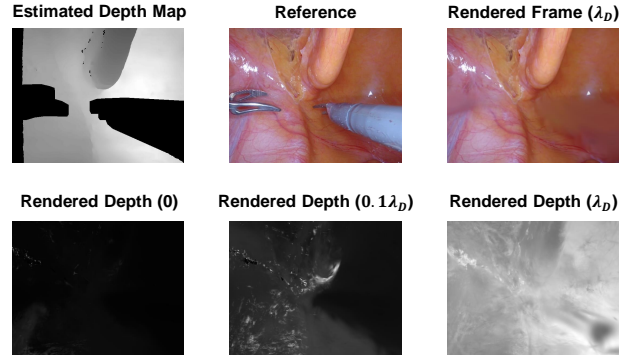


Fig. 3. Ablation on depth regularization. We show rendering depth maps with different depth regularization strength on scene "pulling soft tissues". The values in the bracket denote the weight of the depth regularization loss.

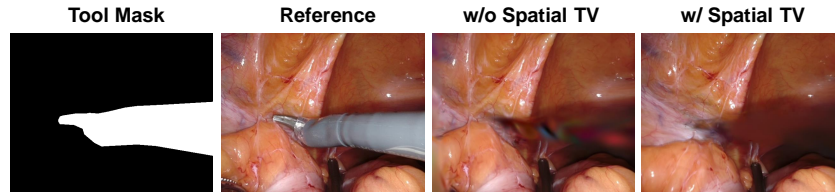


Fig. 4. Ablation on spatial TV loss. We show rendering frames w/ and w/o spatial TV loss on scene "cutting tissues twice".

it infeasible for surgical downstream applications. Second, due to the lack of 3D cues and surface constrains in single-viewpoint videos for Gaussian Splatting optimization, it is likely that artifacts and ambiguities happen in 3D reconstruction with novel viewpoints. Accordingly, future works can focus on practical endoscopic reconstruction with surface-aligned Gaussian Splatting. 3D tissues reconstruction with more surgical cameras is needed to facilitate realistic downstream tasks. Additionally, regularization that encourages the Gaussians to well distributed over the surface can mitigate weaknesses on reconstructed scene surface and geometry, as suggested by [7].

Acknowledgement

We thank Med-AIR Lab CUHK for DaVinci robotic prostatectomy data.

References

1. Batlle, V.M., Montiel, J.M., Fua, P., Tardós, J.D.: Lightneus: Neural surface reconstruction in endoscopy using illumination decline. In: International Conference on Medical Image Computing and Computer-Assisted Intervention. pp. 502–512. Springer (2023)
2. Cao, A., Johnson, J.: Hexplane: A fast representation for dynamic scenes. In: Proceedings of the IEEE/CVF Conference on Computer Vision and Pattern Recognition. pp. 130–141 (2023)
3. Chen, L., Tang, W., John, N.W., Wan, T.R., Zhang, J.J.: Slam-based dense surface reconstruction in monocular minimally invasive surgery and its application to augmented reality. *Computer methods and programs in biomedicine* **158**, 135–146 (2018)
4. Chung, J., Oh, J., Lee, K.M.: Depth-regularized optimization for 3d gaussian splatting in few-shot images. arXiv preprint arXiv:2311.13398 (2023)
5. Fridovich-Keil, S., Meanti, G., Warburg, F.R., Recht, B., Kanazawa, A.: K-planes: Explicit radiance fields in space, time, and appearance. In: Proceedings of the IEEE/CVF Conference on Computer Vision and Pattern Recognition. pp. 12479–12488 (2023)
6. Gao, W., Tedrake, R.: Surfelwarp: Efficient non-volumetric single view dynamic reconstruction. arXiv preprint arXiv:1904.13073 (2019)
7. Guédon, A., Lepetit, V.: Sugar: Surface-aligned gaussian splatting for efficient 3d mesh reconstruction and high-quality mesh rendering. arXiv preprint arXiv:2311.12775 (2023)
8. Kerbl, B., Kopanas, G., Leimkühler, T., Drettakis, G.: 3d gaussian splatting for real-time radiance field rendering. *ACM Transactions on Graphics* **42**(4) (2023)
9. Li, Y., Richter, F., Lu, J., Funk, E.K., Orosco, R.K., Zhu, J., Yip, M.C.: Super: A surgical perception framework for endoscopic tissue manipulation with surgical robotics. *IEEE Robotics and Automation Letters* **5**(2), 2294–2301 (2020)
10. Li, Y., Fu, X., Zhao, S., Jin, R., Zhou, S.K.: Sparse-view ct reconstruction with 3d gaussian volumetric representation. arXiv preprint arXiv:2312.15676 (2023)
11. Li, Z., Liu, X., Drenkow, N., Ding, A., Creighton, F.X., Taylor, R.H., Unberath, M.: Revisiting stereo depth estimation from a sequence-to-sequence perspective with transformers. In: Proceedings of the IEEE/CVF international conference on computer vision. pp. 6197–6206 (2021)
12. Long, Y., Li, Z., Yee, C.H., Ng, C.F., Taylor, R.H., Unberath, M., Dou, Q.: E-dssr: efficient dynamic surgical scene reconstruction with transformer-based stereoscopic depth perception. In: Medical Image Computing and Computer Assisted Intervention—MICCAI 2021: 24th International Conference, Strasbourg, France, September 27–October 1, 2021, Proceedings, Part IV 24. pp. 415–425. Springer (2021)
13. Lu, J., Jayakumari, A., Richter, F., Li, Y., Yip, M.C.: Super deep: A surgical perception framework for robotic tissue manipulation using deep learning for feature extraction. In: 2021 IEEE International Conference on Robotics and Automation (ICRA). pp. 4783–4789. IEEE (2021)
14. Luiten, J., Kopanas, G., Leibe, B., Ramanan, D.: Dynamic 3d gaussians: Tracking by persistent dynamic view synthesis. arXiv preprint arXiv:2308.09713 (2023)
15. Mildenhall, B., Srinivasan, P.P., Tancik, M., Barron, J.T., Ramamoorthi, R., Ng, R.: Nerf: Representing scenes as neural radiance fields for view synthesis. *Communications of the ACM* **65**(1), 99–106 (2021)

16. Newcombe, R.A., Fox, D., Seitz, S.M.: Dynamicfusion: Reconstruction and tracking of non-rigid scenes in real-time. In: Proceedings of the IEEE conference on computer vision and pattern recognition. pp. 343–352 (2015)
17. Park, K., Sinha, U., Barron, J.T., Bouaziz, S., Goldman, D.B., Seitz, S.M., Martin-Brualla, R.: Nerfies: Deformable neural radiance fields. In: Proceedings of the IEEE/CVF International Conference on Computer Vision. pp. 5865–5874 (2021)
18. Pumarola, A., Corona, E., Pons-Moll, G., Moreno-Noguer, F.: D-nerf: Neural radiance fields for dynamic scenes. In: Proceedings of the IEEE/CVF Conference on Computer Vision and Pattern Recognition. pp. 10318–10327 (2021)
19. Ramamoorthi, R., Hanrahan, P.: An efficient representation for irradiance environment maps. In: Proceedings of the 28th annual conference on Computer graphics and interactive techniques. pp. 497–500 (2001)
20. Recasens, D., Lamarca, J., Fácil, J.M., Montiel, J., Civera, J.: Endo-depth-and-motion: Reconstruction and tracking in endoscopic videos using depth networks and photometric constraints. *IEEE Robotics and Automation Letters* **6**(4), 7225–7232 (2021)
21. Schonberger, J.L., Frahm, J.M.: Structure-from-motion revisited. In: Proceedings of the IEEE conference on computer vision and pattern recognition. pp. 4104–4113 (2016)
22. Scott, D.J., Cendan, J.C., Pugh, C.M., Minter, R.M., Dunnington, G.L., Kozar, R.A.: The changing face of surgical education: simulation as the new paradigm. *Journal of Surgical Research* **147**(2), 189–193 (2008)
23. Shin, C., Ferguson, P.W., Pedram, S.A., Ma, J., Dutson, E.P., Rosen, J.: Autonomous tissue manipulation via surgical robot using learning based model predictive control. In: 2019 International conference on robotics and automation (ICRA). pp. 3875–3881. IEEE (2019)
24. Song, J., Wang, J., Zhao, L., Huang, S., Dissanayake, G.: Dynamic reconstruction of deformable soft-tissue with stereo scope in minimal invasive surgery. *IEEE Robotics and Automation Letters* **3**(1), 155–162 (2017)
25. Wang, Y., Long, Y., Fan, S.H., Dou, Q.: Neural rendering for stereo 3d reconstruction of deformable tissues in robotic surgery. In: International Conference on Medical Image Computing and Computer-Assisted Intervention. pp. 431–441. Springer (2022)
26. Wu, G., Yi, T., Fang, J., Xie, L., Zhang, X., Wei, W., Liu, W., Tian, Q., Wang, X.: 4d gaussian splatting for real-time dynamic scene rendering. arXiv preprint arXiv:2310.08528 (2023)
27. Yang, C., Wang, K., Wang, Y., Dou, Q., Yang, X., Shen, W.: Efficient deformable tissue reconstruction via orthogonal neural plane. arXiv preprint arXiv:2312.15253 (2023)
28. Yang, C., Wang, K., Wang, Y., Yang, X., Shen, W.: Neural lerplane representations for fast 4d reconstruction of deformable tissues. arXiv preprint arXiv:2305.19906 (2023)
29. Yang, Z., Yang, H., Pan, Z., Zhu, X., Zhang, L.: Real-time photorealistic dynamic scene representation and rendering with 4d gaussian splatting. arXiv preprint arXiv:2310.10642 (2023)
30. Yang, Z., Gao, X., Zhou, W., Jiao, S., Zhang, Y., Jin, X.: Deformable 3d gaussians for high-fidelity monocular dynamic scene reconstruction. arXiv preprint arXiv:2309.13101 (2023)
31. Zha, R., Cheng, X., Li, H., Harandi, M., Ge, Z.: Endosurf: Neural surface reconstruction of deformable tissues with stereo endoscope videos. In: International

- Conference on Medical Image Computing and Computer-Assisted Intervention. pp. 13–23. Springer (2023)
32. Zhou, H., Jagadeesan, J.: Real-time dense reconstruction of tissue surface from stereo optical video. *IEEE transactions on medical imaging* **39**(2), 400–412 (2019)
 33. Zhou, H., Jayender, J.: Emdq-slam: Real-time high-resolution reconstruction of soft tissue surface from stereo laparoscopy videos. In: *Medical Image Computing and Computer Assisted Intervention–MICCAI 2021: 24th International Conference, Strasbourg, France, September 27–October 1, 2021, Proceedings, Part IV* 24. pp. 331–340. Springer (2021)
 34. Zwicker, M., Pfister, H., Van Baar, J., Gross, M.: Surface splatting. In: *Proceedings of the 28th annual conference on Computer graphics and interactive techniques*. pp. 371–378 (2001)